Model predictive control for isolated DC/DC power converters with transformer peak current shaving

Linglin Chen*, Luca Tarisciotti, Alessandro Costabeber, Pat Wheeler, Pericle Zanchetta
Department of Electrical and Electronics Engineering
University of Nottingham
*eexlc15@nottingham.ac.uk

***Abstract*— In this paper a Model Predictive Control, suitable for isolated DC/DC power converters and featuring optimization on converter operations, is proposed. The control is designed based on a specific a current-fed DC/DC converter topology, named Active-Bridge-Active-Clamp converter. This topology is particularly suitable for batteries interface, utilizing its interleaved structure in order to achieve an effective current ripple cancellation at the low voltage terminals. However, the increased complexity of the ABAC converter requires a specific modulation implementation and a detailed converter modeling. For such reasons, the operating principle of the ABAC converter is firstly introduced and mathematical models of the ABAC are developed in this paper. Subsequently, a Model Predictive Control is proposed and implemented aiming to achieve terminal current regulation, improve dynamic performance and reduce current stress in a wide DC voltage operating range, whilst maintaining a fixed switching frequency and a reduced prediction horizon. Simulation results for a 10kW ABAC converter are provided to validate the theoretical claims.**

Keywords—Model Predictive Control (MPC), Isolated DC/DC power converter.

I. INTRODUCTION

A DC voltage level of 270V is currently being adopted in modern civil aircrafts [1] like, for example, the Airbus A380 and the Boeing B-787 and in fighters like the Lockheed Martin F-35. Many large aircrafts use a combination of voltage levels, with 28VDC frequently being used to power flight critical avionics [2], to interface with batteries or fuel cells [3]. Therefore, a high step up/down DC/DC converter is needed to interface the high and low DC buses.

Amongst other DC/DC converters [4], Dual-Active-Bridge (DAB) is often investigated for its bidirectional power flow and galvanic isolation [3]. The DAB also features high efficiency when input and output voltages are kept at their nominal values, benefited from the inherent Zero Voltage Switching (ZVS) in all switches on both sides of the transformer [5]. However, large current ripple is expected on the Low Voltage (LV) converter side [6], requiring large passive filters. In addition, active suppression techniques are needed to mitigate potential resonances between LV terminal and LV source/load [7]. Deriving from the S-DAB proposed in [8], a current-fed DAB named Active-Bridge-Active-Clamp (ABAC) is introduced in papers [9]–[11]. The term active bridge describes the full H-Bridge on the primary side of the transformer, and active clamps describe the four clamping circuits on the secondary side of the transformer. The ABAC topology provides bidirectional power transfer ability and extra degree of freedom to effectively cancel the LV side current ripple. Furthermore, in terms of efficiency and power density, the ABAC converter represents a viable alternative to classical DAB in MEA applications [9], [12]. The ABAC converter can be intuitively modulated in a single phase shift mode mentioned in [13]. Although the application of this modulation is straightforward, it presents many disadvantages at light load and, in general, in operating condition different from the nominal one. Therefore, Phase-Shift-Modulations (PSM) are investigated in [11]. However, the transformer voltage DC bias and output currents DC variations may be present in the ABAC converter. These effects can be mitigated by a specific modulation design [11].

On the other hand Model Predictive Control (MPC) may offer a cost effective solution for this application, allowing online calculation of the optimal converter operating point. In fact, MPC is often considered for power electronics converter control for the several advantages it can provide, such as easy inclusion of nonlinearities and constraints, fast dynamics and simple digital implementation. In particular, Finite Control Set Model Predictive Control (FCS-MPC) has been intensively investigated in AC power conversion [14]–[16]. The applications of MPC in DC/DC converters are reported in [17]–[21]; The authors in [17], [21] propose the implementation of FCS-MPC in a boost converter with the receding horizon. However this approach results in a larger current ripple than a PI-PWM based approach. In [18], authors have compared a Continuous Control Set MPC (CCS-MPC) with a hysteresis control in a boost converter. Although the dynamics performances are similar in those two control approaches, the voltage overshoot is completely avoided by using CCS-MPC control. In [19] a single step prediction CCS-MPC is implemented, together with an outer PI loop to regulate the output voltage of a buck converter. This shows better response performance than a PI-PWM based control. The authors in [20] include switching losses and transformer current Root-Mean-Square (RMS) value into the cost function, which is evaluated for different modulation techniques. This approach can achieve optimal efficiency in a wide operating range, but it presents similar dynamics performance to PI controllers.

This paper is organised as follow: in Section II, the operation principle of the ABAC converter featuring the improved PSM techniques is briefly introduced. In Section III, the average model, small signal model and discrete models of the ABAC converter are presented. In Section IV, a MPC aiming to regulate LV current is proposed and described in detail. Validations to the theoretical claims are carried out in simulation presented in Section V. Finally Section VI concludes the paper.

II. OPERATION PRINCIPLES WITH PSM

The schematic of the ABAC converter is presented in Fig. 1. A full H-Bridge is connected to the HV side of the transformer while four clamp half bridge circuits are configured at LV side. The four clamp circuits together with four LV side output inductors construct an interleaved structure similar to the multiphase interleaved boost converter [22]. Current ripple on I_{LV} can be effectively cancelled if proper modulation is applied [11] for the ABAC converter.

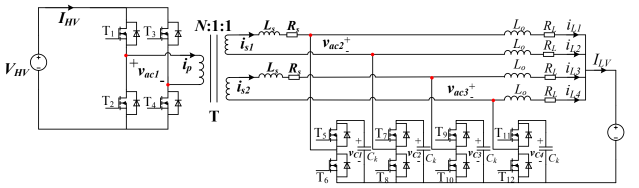

Fig. 1. The schematic of the ABAC converter.

The Phase Shift Modulation (PSM) technique applied to this converter is described in Fig. 2 where all the relevant waveform are shown [11]. Using this modulation technique DC voltage offset at the transformer terminals are suppressed as well as unbalances in the output inductors currents. It is also important to highlight that duty cycle of all the switches over one switching period is fixed at 50%. As a result the clamp capacitors voltage V_c presents a steady state voltage equal to twice the LV side terminal voltage V_{LV}, i.e. V_c=2V_{LV}.

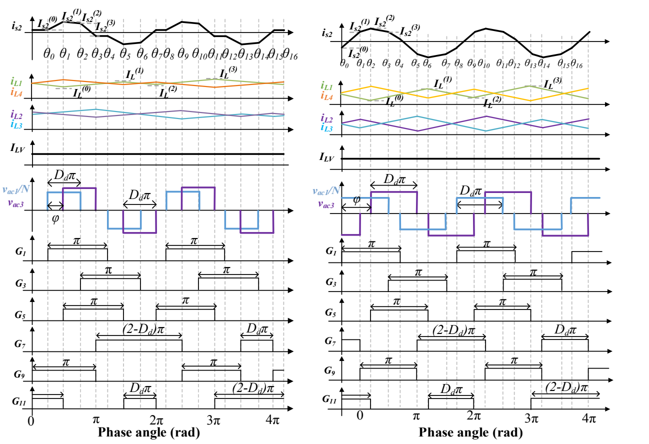

(a) (b)

Fig. 2. Typical waveforms for operation (a) 0<φ/π<Min{1-D_d,D_d} (Mode IV) and (b) 1-D_d<φ/π<D_d (Mode III) using the proposed PSM scheme where G_1-G_{12} drive T_1-T_{12} with G_4=G_1, G_2=G_3=not(G_1), G_6=not(G_5), G_8=not(G_7), G_{10}=not(G_9) and G_{12}=not(G_{11}).

As can be seen from Fig. 2, taking G_7 as an example, the sum of the active period in one switching cycle is π. It is important to highlight that since the switches T_7 (driven by signal G_7) and T_9 (driven by signal G_9) are always complementarily switched, therefore the LV currents i_{L2} and i_{L3} are always interleaved. The same behaviour can be observed on switches T_5 and T_{11}. Therefore, I_{LV} ideally does not present any current ripple at any operating points. In the meantime, the clamp circuits generate also the transformer secondary port voltages v_{ac2}, v_{ac3}. The combinations of G_5 and G_7 also G_9 and G_{11} are used to generate v_{ac2} and v_{ac3}, respectively. Specifically, taking the upper secondary as an example, the transformer secondary voltage v_{ac2} can be generated as v_{ac2}=$v_{c1}G_5$-$v_{c2}G_7$. In half switching cycle, the active states of both voltages v_{ac1} and v_{ac3}, v_{ac3} present the same period of πD_d, where D_d can vary from 0 to 1Additionally the outer phase shift φ between transformer primary and secondary voltages, can be varied from 0 to 2π. D_d and φ can be independently controlled in order to optimize the operation of the converter.

The power contour plot of the ABAC is shown in Fig. 3 [23], featuring power transfer from HV to LV sources. Although bidirectional power flow is also possible, it is not discussed in this paper for brevity. The operation of the converter is divided into four regions. Each region represents a different mode of operation. However, the converter is predominately working in Mode III and Mode IV due to significant loss increase in Mode I and II. As can be seen from Fig. 3, along each power contour line, numerous combinations of φ and D_d exist to transfer the same power. This provides the degree of freedom to optimize the operation of the ABAC converter with PSM. Although many optimization objectives are possible [24]–[26], transformer peak current is selected as our minimization target.

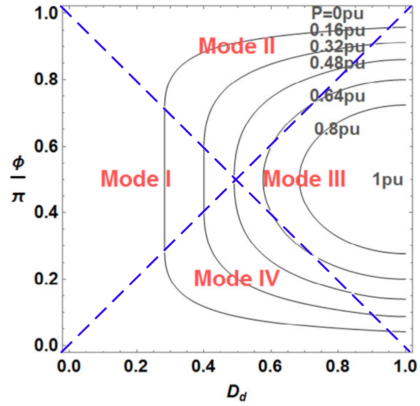

Fig. 3. Power contour plot of the ABAC with illustration on constraints of differnet operation modes.

III. Modelling of the ABAC

The small signal model and the discrete model of the ABAC converter, which are needed for the PI and MPC control design, are derived in this section. Firstly, a switching average model is developed as shown in Fig. 4 where state variables and the controllable current sources are highlighted in red and violet, respectively. In particular i_{C1}-i_{C4} are controlled by varying φ and D_d. It is important to highlight that the switching average is carried out in two switching period $2T_s$ due to the feature of the PSM shown in Fig. 2.

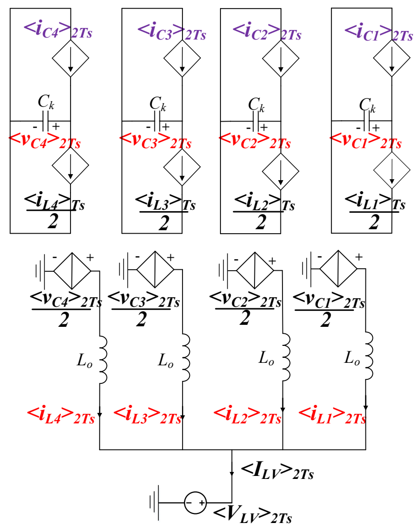

Fig. 4. The averaged model of the ABAC converter.

The dynamic and output equations of the ABAC converter are illustrated in equations (1) and (2).

$$\begin{cases} \dfrac{d < v_{Cm} >_{2T_s}}{dt} = f_{1m} = -\dfrac{1}{2C_k} < i_{Lm} >_{2T_s} + \dfrac{1}{C_k} < i_{Cm} >_{2T_s} \\ \dfrac{d < i_{Lm} >_{2T_s}}{dt} = f_{2m} = \dfrac{1}{2L_o} < v_{Cm} >_{2T_s} - \dfrac{1}{L_o} < V_{LV} >_{2T_s} \end{cases} \quad (1)$$
$(m = 1,2,3,4)$

$$< I_{LV} >_{2T_s} = \begin{pmatrix} 0 & 0 & 0 & 0 & 1 & 1 & 1 & 1 \end{pmatrix} \begin{pmatrix} < v_{C1} >_{2T_s} \\ < v_{C2} >_{2T_s} \\ < v_{C3} >_{2T_s} \\ < v_{C4} >_{2T_s} \\ < i_{L1} >_{2T_s} \\ < i_{L2} >_{2T_s} \\ < i_{L3} >_{2T_s} \\ < i_{L4} >_{2T_s} \end{pmatrix} \quad (2)$$

The expression of the controllable current sources depends on the mode of operation as illustrated in Fig. 2 and Fig. 3. Taking Mode IV in Fig. 2(a) as an example, the controllable current source can be derived as:

$$< i_{Cm} >_{2T_s} = \frac{\int_{\theta_1}^{\theta_5} i_{s2}(\theta) d\theta + \int_{\theta_7}^{\theta_{11}} i_{s2}(\theta) d\theta}{2T_s} = \frac{\int_{\theta_1}^{\theta_3} i_{s2}(\theta) d\theta}{T_s} \quad (3)$$

Therefore, the expressions for each mode can be calculated based on (3) as:

$$< i_{Cm\_IV} >_{2T_s} = \frac{1}{8Nf_s L_s} < V_{HV} >_{2T_S} D_\varphi (2D_d - D_\varphi) \quad (4)$$

$$< i_{Cm\_III} >_{2T_s} = \frac{1}{8Nf_s L_s} < V_{HV} >_{2T_S} [2D_\varphi - 2\, D_\varphi^{\,2} - (D_d - 1)^2] \quad (5)$$

where, m represent the index 1 to 4, D_φ is defined as φ/π and f_s is the switching frequency.

A. The small signal model of the ABAC converter

The small signal model of the ABAC converter is derived in this subsection. The values of the two control variables D_d and φ are chosen in order to minimize transformer peak current. This optimization is carried out offline, thus reducing the number of control variables required in the controller design, which is described in the following section. The control variables trajectories which minimize the peak transformer current are shown in Fig. 5. The relationships between D_d and φ are derived as follows:

$$D_\varphi = \begin{cases} \dfrac{2r_V - 1}{2r_V + 1} D_d, & D_d < \dfrac{2r_V + 1}{4r_V} \\ \dfrac{1}{2r_V - 1} D_d + \dfrac{3 - 2r_V}{2 - 4r_V}, & D_d > \dfrac{2r_V + 1}{4r_V} \end{cases} \quad \text{when } r_V > 0.5 \quad (6)$$

$$D_\varphi = \begin{cases} \dfrac{1 - 2r_V}{1 + 2r_V} D_d, & D_d < \dfrac{1 + 2r_V}{2} \\ \dfrac{2r_V}{1 - 2r_V} D_d + \dfrac{6r_V - 1}{4r_V - 2}, & D_d > \dfrac{1 + 2r_V}{2} \end{cases} \quad \text{when } r_V < 0.5 \quad (7)$$

where, r_V is defined as the voltage ratio NV_{LV}/V_{HV}.

Substituting equations (6) and (7) into equation (1), and performing a Jacobian linearization of the model, the following small signal state space matrix is obtained:

$$\begin{pmatrix} d\,\tilde{v}_{C1}/dt \\ \vdots \\ d\,\tilde{i}_{L1}/dt \\ \vdots \end{pmatrix} = A \begin{pmatrix} \tilde{v}_{C1} \\ \vdots \\ \tilde{i}_{L1} \\ \vdots \end{pmatrix} + B\,\tilde{D}_d \quad (8)$$

$$A = \begin{pmatrix} \dfrac{\partial f_{11}}{\partial < v_{c1} >_{T_s}}\Big|_{\bar{v}_{cm}} & \cdots & \dfrac{\partial f_{11}}{\partial < i_{L1} >_{T_s}}\Big|_{\bar{i}_{Lm}} & \cdots \\ \vdots & \vdots & \vdots & \vdots \\ \dfrac{\partial f_{21}}{\partial < v_{c1} >_{T_s}}\Big|_{\bar{v}_{cm}} & \cdots & \dfrac{\partial f_{21}}{\partial < i_{L1} >_{T_s}}\Big|_{\bar{i}_{Lm}} & \cdots \\ \vdots & \vdots & \vdots & \vdots \end{pmatrix} \quad (9)$$

$$B = \begin{pmatrix} \dfrac{\partial f_{11}}{\partial D_d}\Big|_{\bar{D}_d} & \cdots & \dfrac{\partial f_{21}}{\partial D_d}\Big|_{\bar{D}_d} & \cdots \end{pmatrix}^T \quad (10)$$

Finally, the open loop transfer function is defined as:

$$G = \frac{\tilde{I}_{LV}}{\tilde{D}_d} \quad (11)$$

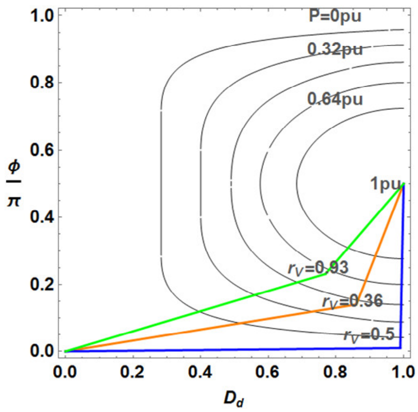

Fig. 5. Minimzed transforemer peak current trajectories

In order to validate the analytical small signal model, Fig. 6 shows the analytical bode plots of *G*, compared with the simulated non-linear model response in 100 different frequencies, using circuit parameters illustrated in Table I. The results shows good matching between the models.

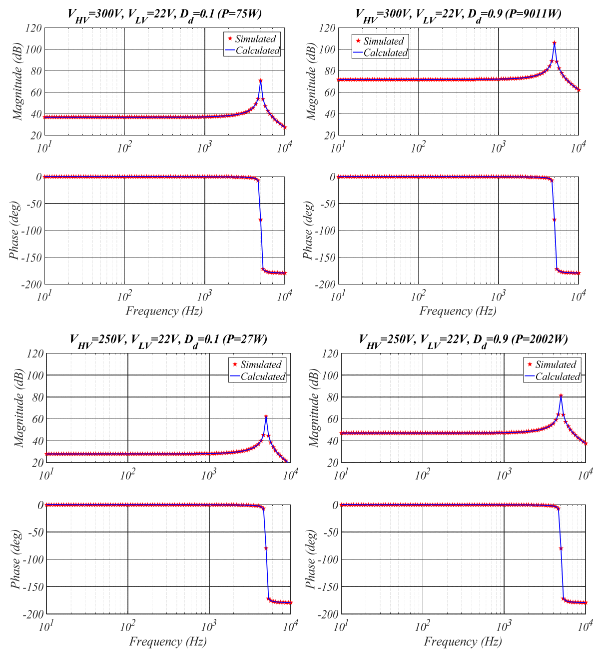

Fig. 6. Open loop bode plot of converter transfer function from the control variable to the output.

From Fig.6 it can be noted a resonance peak at high frequency, which is caused by the resonance between clamp capacitors and output inductors. According to Nyquist stability criteria, the PI controller has to suppress this peak amplitude below 0db to ensure stability. As can also be observed from the Fig. 6, the small signal model varies under different operating conditions. The variation in the small signal model requires different design of the PI parameters at each operating point in order to ensure fast dynamic performances and stability. For above reasons, a globally designed controller is desired in the ABAC converter when wide voltage operating range is desired.

B. The discrete model of the ABAC converter

The aim of the designed MPC controller is to regulate the LV converter side current I_{LV} at a desired reference value. The averaged model of (1) is modified into (12).

$$\frac{d^2 < I_{LV} >_{2T_s}}{dt^2} = -\frac{1}{4L_oC_k} < I_{LV} >_{2T_s} + \frac{1}{2L_oC_k}\sum_{m=1}^{4} < i_{Cm} >_{2T_s} \tag{12}$$

Therefore, the Euler backward discretization to equation (12) can be carried out and the instantaneous LV current can be predicted as:

$$I_{LV}[k+1] = \lambda_1 I_{LV}[k] + \lambda_2 I_{LV}[k-1] + \lambda_3 \sum_{m=1}^{4} i_{Cm}[k] \tag{13}$$

where

$$\lambda_1 = 2 - \frac{1}{4C_kL_of_s^{\,2}},\quad \lambda_2 = -1,\quad \lambda_3 = \frac{1}{2C_kL_of_s^{\,2}} \tag{14}$$

$$\sum_{m=1}^{4} i_{Cm\_M5}[k] = \frac{1}{2Nf_sL_s} V_{HV}[k]D_\varphi[k](2D_d[k] - D_\varphi[k]) \tag{15}$$

$$\sum_{m=1}^{4} i_{Cm\_M6}[k] = \frac{1}{2Nf_sL_s} V_{HV}[k](2\mathrm{D}_\varphi[\mathrm{k}]\text{-}2\ \mathrm{D}_\varphi^{\ 2}[\mathrm{k}]\text{-}(\mathrm{D_d}[\mathrm{k}]\text{-}1)^2) \tag{16}$$

By imposing equation (12) equal to zero, the steady state LV current $I_{LV}^{*}[k]$ is obtained as follows:

$$I_{LV}^{\ *}[k] = 2\sum_{m=1}^{4} i_{Cm}[k] \tag{17}$$

For the MPC design described in the next section the derivative of D_d with respect to D_φ at constant power is also required and calculated as follows:

$$\frac{\Delta D_d}{\Delta D_\varphi}\bigg|_{P=P_{const}} \begin{cases} \dfrac{\partial P(D_d,D_\varphi)/\partial D_\varphi}{\partial P(D_d,D_\varphi)/\partial D_d} = \dfrac{1-D_d}{2D_\varphi - 1}, \text{ModeIII} \\ \dfrac{\partial P(D_d,D_\varphi)/\partial D_\varphi}{\partial P(D_d,D_\varphi)/\partial D_d} = \dfrac{D_\varphi}{D_\varphi - D_d}, \text{ModeIV} \end{cases} \tag{18}$$

Similarly the derivative of D_d with respect to D_φ at constant transformer peak current is calculated as follows:

$$\frac{\Delta D_d}{\Delta D_\varphi}\bigg|_{I_{peak}=I_{peak\_const}} = \frac{\partial I_{peak}(D_d,D_\varphi)/\partial D_\varphi}{\partial I_{peak}(D_d,D_\varphi)/\partial D_d} = \begin{cases} \dfrac{1}{2} - \dfrac{V_{HV}}{4NV_{LV}}, r_V < 0.5 \\ \dfrac{1}{2} - \dfrac{NV_{LV}}{V_{HV}}, r_V > 0.5 \end{cases} \tag{19}$$

IV. THE PROPOSED MPC

Based on the model developed in Section III.B, the cost function is thus derived as follows:

$$\begin{aligned} ct = {} & \alpha_1(I_{LVref} - I_{LV}^{\ *}[k+2])^2 + \alpha_2(I_{LV}[k+2] - I_{LV}[k+1])^2 \\ & + \alpha_3\Big(\frac{\Delta D_d}{\Delta D_\varphi}\Big|_{P=P_{const}} - \frac{\Delta D_d}{\Delta D_\varphi}\Big|_{I_{peak}=I_{peak\_const}}\Big)^2 \end{aligned} \tag{20}$$

where, I_{LVref} is the LV current reference value and α_1, α_2, α_3 are weighing factors that are selected empirically.

The two control variables D_d and D_φ that minimize the cost function (20), can be obtained from the proposed MPC controller with D_φ ranges from 0 to 1 for buck operations, and D_d ranges from 0 to 1. In order to achieve a control algorithm which is practically implementable on standard commercial microcontrollers, the proposed MPC evaluates a limited control variable set at each sampling instant, with a prediction horizon of two sampling period, in order to take into account the computational delay. In fact, if control precision (the smallest phase shift value that can be controlled in digital controllers) of Δ_d is defined, there are $N_\varphi = \pi/\Delta_d$ and $N_d = \pi/\Delta_d$ points to be evaluated for both variables respectively. A total number of $N_\varphi * N_d$ points have to be evaluated in each control cycle. This is usually not feasible in practical implementations. Alternatively, in one control period, only a limited control variables set of 9 points is assessed around the previous operating point (a, b) as shown in Fig. 7.

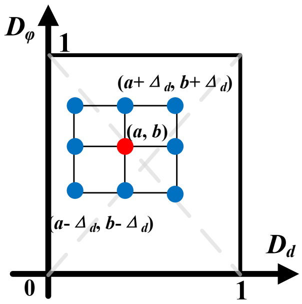

Fig. 7. The minial search span of the control variables.

In the proposed cost function (20), the first term regulates the steady state current to the reference value. The reason for not using the instantaneous current is to avoid oscillation in steady state caused by the resonance between clamp capacitors and output inductors as indicated in Fig. 6. However, applying solely the first term, overshoot in the controller step response may be present. Aiming to suppress the overshoot, the second term is proposed in the cost function (20). Essentially, the second term limit the slope of I_{LV} [27], in order to avoid the effects of the resonance between clamp capacitors and output inductors during transients. The third term is implemented to minimize the peak transformer current value. Minimal peak current points can be found at the tangent points of the constant power contour lines and the peak current contour lines. It can be demonstrated that the cost function in (20) present only one equilibrium point for each operating conditions, related to the control variable trajectories of Fig. 5.

V. SIMULATION RESULTS

The proposed MPC controller is designed and implemented in PLECS. The control diagram is shown in Fig. 8 with the circuit parameters listed in Table I. Only terminal voltages on the HV and LV side, together with the LV terminal current need to be measured. The LV current I_{LV} is controlled to follow its reference value I_{LVref}. The controller outputs are the phase shifts D_d and D_φ necessary to implement the PSM already described in Fig. 2. These phase shifts are then fed into the modulation algorithm, which generates the driving signals G_1-G_{12}. This MPC controller is developed based on the system global parameters, suitable for the operating ranges listed in Table I. The control implementation is straightforward and requires only the online calculation of equations (13), (17), (18), (19) and (20) for the desired control set. Considering a minimal control set of 9 points, as illustrated in Fig. 7, the computational burden is reduced when compared to other MPC techniques, which requires a long prediction horizon [17], [21]. The weighing factors are empirically designed as α_1=1, α_2= 60, α_3= 50.

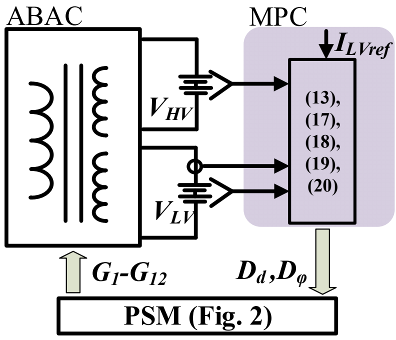

Fig. 8. The control block of the proposed MPC in the ABAC converter.

Table I
CONVERTER KEY PARAMETERS

Symbol	Description	Value
V_{HV}	HV range	170-300 V
V^*_{HV}	Nominal HV voltage	270V
V_{LV}	LV range	22-30 V
V^*_{LV}	Nominal LV voltage	28V
P^*	Rated power	10 kW
f_s	Switching frequency	100 kHz
N	Transformer turn ratio	5
C_k	Clamp capacitance	150 uF
L_s	Power transfer inductance	500 nH
L_o	Output inductance	1.65 uH

A. The dynamic performance of the proposed MPC

The dynamic performance using the proposed MPC is simulated under different voltage conditions shown in Fig. 9. It can be observed that there are no overshoot in the controlled variable I_{LV}. The controller presents fast dynamic performances for the application, with the longest settling time equal to 3.9ms in the simulation.

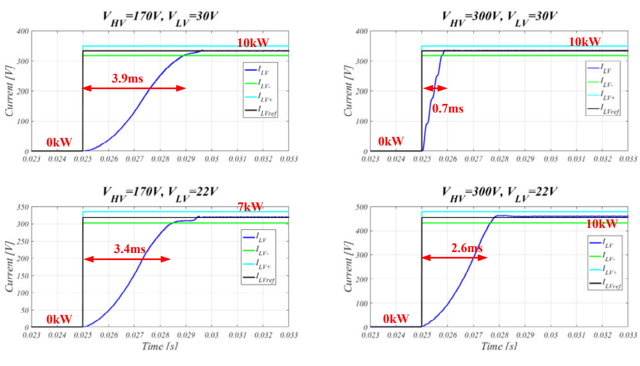

Fig. 9. Transitions under different voltage operaing conditions using the proposed MPC. I_{LV-} and I_{LV+} are the 95% and 105% limit with respect to the reference I_{LVref}.

It is worth mentioning that, if faster dynamic is required in other applications, the control set can be increased. However the computational burden increase accordingly to the control set size, and more advanced digital control platforms may be required.

B. Comparison of using instantaneous model and steady state model

If the instantaneous current model (13) is used to track the reference value in the cost function as illustrated in (21), large oscillation on the LV current is present as shown in Fig. 10.

$$
\begin{aligned}
ct &= \alpha_1 (I_{LV\,ref} - I_{LV}[k+2])^2 \\
&+ \alpha_3 \left(\frac{\Delta D_d}{\Delta D_\varphi}\Big|_{P=P_{const}} - \frac{\Delta D_d}{\Delta D_\varphi}\Big|_{I_{peak}=I_{peak\_const}} \right)^2
\end{aligned} \tag{21}
$$

It can be noted from Fig. 10 that the steady state oscillation frequency correspond to the resonance frequency already analysed in Fig. 6.

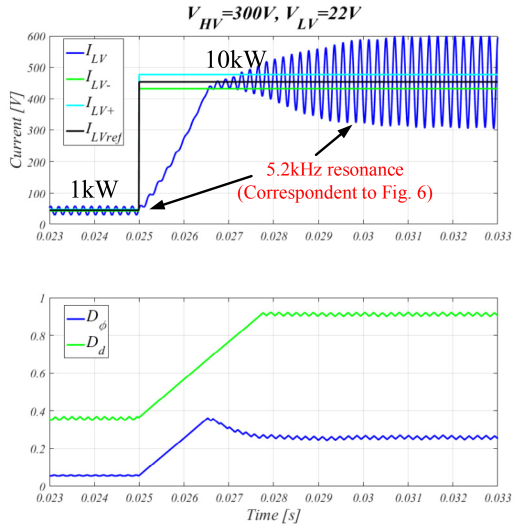

Fig. 10. The oscillation issue by using instantaneous current in the first term of the cost function. I_{LV-} and I_{LV+} are the 95% and 105% limit with respect to the reference I_{LVref}.

For such reason, the steady state model of equation (17) is implemented in the controller using the cost function already described in equation (20). In fact, using the proposed MPC controller the steady state oscillations are suppressed as shown in Fig. 11.

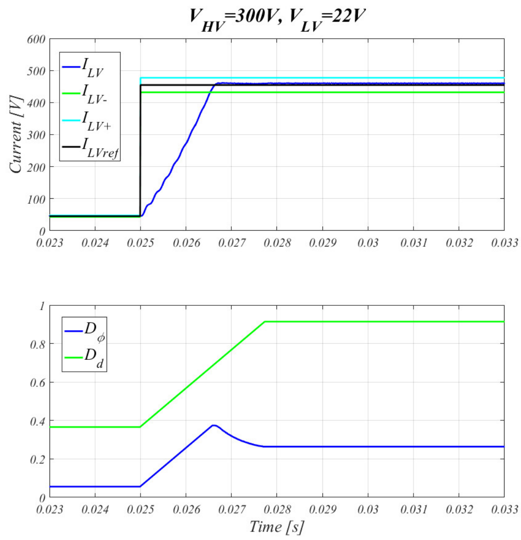

Fig. 11. The propsoed MPC using steady state model in the first term of the cost function (20). I_{LV-} and I_{LV+} are the 95% and 105% limit with respect to the reference I_{LVref}.

C. Effectiveness of the second term-overshoot suppression

When a larger control set is used, as discussed in Section V.A, the transient response can be improved, as shown in middle plot of Fig. 12. However, this may result in a current overshoot during transients. This effect is also caused by the resonance between clamp capacitors and output inductors, as already discussed in Section III.A and V.B. Therefore, the second cost function term is used to limit the current variation over one sampling period. Simulation results including this cost function term and using a control variables set of 9 and 441 points are also shown in the upper and lower plot of Fig. 12, respectively. When the second term is enabled, it can be noticed that overshoot and oscillations are eliminated, resulting in fast dynamic performances which mainly depends of the computational burden allowed by the practical implementation.

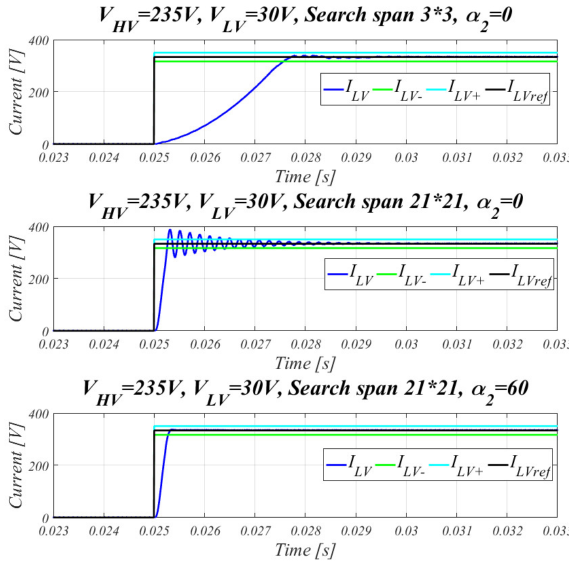

Fig. 12. Dynamic improvement by increasing the search span, and verification of the effectiveness of the second term. I_{LV-} and I_{LV+} are the 95% and 105% limit with respect to the reference I_{LVref}.

D. Effectiveness of the third term-peak current shaving

Fig. 13 shows a transition from 0kW to 10kW under voltage condition 300V/22V. It can be observed that from point A to point B, the I_{LV} presents small oscillations around its steady state value, while the transformer peak current is being reduced. Fig. 14 shows the trajectory of the two control variables. Firstly D_d and D_φ are increased linearly, in order to reach the desired I_{LV} value. During this interval, the first term in (20) has the highest impact on the cost function. However, when I_{LV} reaches its reference value I_{LVref}, the first term in (20) presents a lower value than the third cost function term (from A to B in Fig. 14) and the transformer peak current is effectively reduced. Additional simulation results are shown in Fig. 15, where the ABAC converter is operated considering 170V and 28V terminal voltages and 1kW power transferred in buck mode. In Fig. 15 the third cost function term is firstly disabled by setting the weighing factor α_3 to zero. When this term is enabled, a transformer peak current reduction can be observed. The correspondent operation trajectory is shown in Fig. 16 where the operating point slides from C to D on the power contour line as illustrated in Fig. 3 to find the minimal transformer peak operating point.

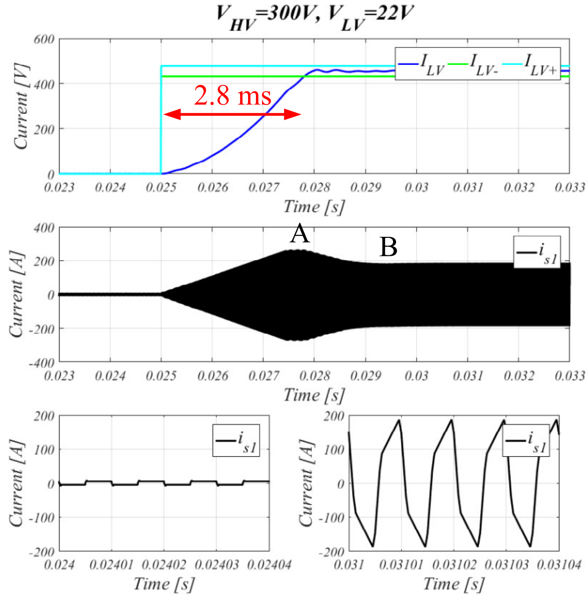

Fig. 13. Transformer peak current shaving from A to B. Workding under 300V/22V voltage condition ,and transition is perfomed from 0kW to 10kW. I_{LV-} and I_{LV+} are the 95% and 105% limit with respect to the reference I_{LVref}.

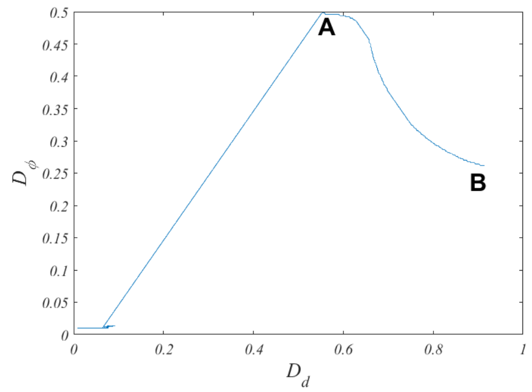

Fig. 14. Demostration on the transition trajectory accorspondant to Fig. 9.

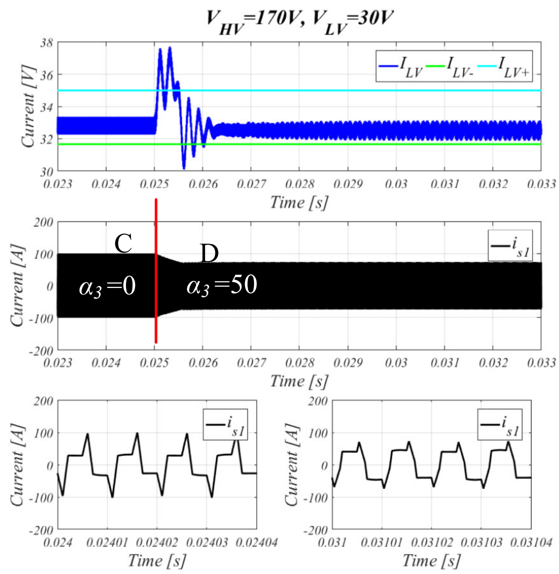

Fig. 15. Transformer peak current shaving from C to D. Working under 170V/30V and 1kW. I_{LV-} and I_{LV+} are the 95% and 105% limit with respect to the reference I_{LVref}.

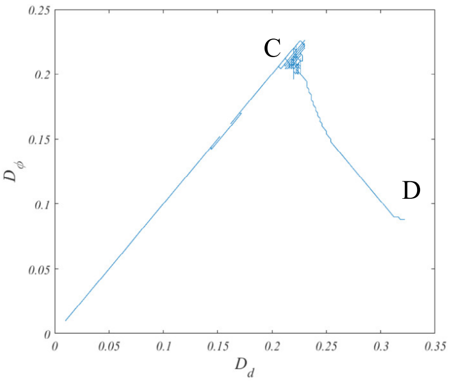

Fig. 16. Demostration on the transition trajectory accorspondant to Fig. 11.

VI. Conclusions

In this paper, a MPC technique is proposed with the aim of controlling the LV converter side current. The proposed technique is particularly suitable for applications where the converter model changes accordingly to different operating conditions, such for the ABAC converter presented in this paper. Moreover the proposed controller presents fast transient response without noticeable overshoot and it is capable of optimizing various control objectives when enough degree of freedom are provided by the system. The proposed MPC controller presents a straightforward implementation on commercial control platforms and is applicable to other isolated DC/DC power converters topologies especially suitable for isolated DC/DC converters such as Dual Active Bridge, Triple Active Bridge and many others.

References

[1] C. Li *et al.*, "A Modified Neutral-Point Balancing Space Vector Modulation Technique for Three-Level Neutral Point Clamped Converters in High Speed Drives," *IEEE Trans. Ind. Electron.*, pp. 1–1, 2018.

[2] P. Wheeler and S. Bozhko, "The More Electric Aircraft," *IEEE Electrif. Mag.*, vol. 2, no. 4, pp. 6–12, 2014.

[3] G. Buticchi, L. Costa, and M. Liserre, "Improving System Efficiency for the More Electric Aircraft: A Look at dc\/dc Converters for the Avionic Onboard dc Microgrid," *IEEE Ind. Electron. Mag.*, vol. 11, no. 3, pp. 26–36, Sep. 2017.

[4] M. Forouzesh, Y. P. Siwakoti, S. A. Gorji, F. Blaabjerg, and B. Lehman, "Step-Up DC–DC Converters: A Comprehensive Review of Voltage-Boosting Techniques, Topologies, and Applications," *IEEE Trans. Power Electron.*, vol. 32, no. 12, pp. 9143–9178, Dec. 2017.

[5] M. H. Kheraluwala, R. W. Gascoigne, D. M. Divan, and E. D. Baumann, "Performance characterization of a high-power dual active bridge DC-to-DC converter," *IEEE Trans. Ind. Appl.*, vol. 28, no. 6, pp. 1294–1301, 1992.

[6] C. Mi, H. Bai, C. Wang, and S. Gargies, "Operation, design and control of dual H-bridge-based isolated bidirectional DC-DC converter," *IET Power Electron.*, vol. 1, no. 4, pp. 507–517, 2008.

[7] J. Riedel, D. G. Holmes, B. P. McGrath, and C. Teixeira, "Active Suppression of Selected DC Bus Harmonics for Dual Active Bridge DC–DC Converters," *IEEE Trans. Power Electron.*, vol. 32, no. 11, pp. 8857–8867, Nov. 2017.

[8] D. Sha, F. You, and X. Wang, "A High Efficiency Current Fed Semi Dual Active Bridge DC-DC Converter for Low Input Voltage Applications," *IEEE Trans. Ind. Electron.*, pp. 1–1, 2015.

[9] L. Tarisciotti, A. Costabeber, C. Linglin, A. Walker, and M. Galea, "Evaluation of isolated DC/DC converter topologies for future HVDC aerospace microgrids," in *2017 IEEE Energy Conversion Congress and Exposition (ECCE)*, 2017, pp. 2238–2245.

[10] L. Chen, L. Tarisciotti, A. Costabeber, P. Zanchetta, and P. Wheeler, "Parameters mismatch analysis for the Active-Bridge-Active-Clamp (ABAC) converter," in *2017 IEEE Southern Power Electronics Conference (SPEC)*, 2017, pp. 1–6.

[11] L. Chen, L. Tarisciotti, A. Costabeber, P. Zanchetta, and P. Wheeler, "Advanced modulation for the Active-Bridge-Active-Clamp (ABAC) converter," in *2017 IEEE Southern Power Electronics Conference (SPEC)*, 2017, pp. 1–6.

[12] D. Urciuoli, R. A. Wood, and C. W. Tipton, "Trade Study and Design of a TRL-4, 100 °C, 28- to 600-V Bidirectional DC." 01-Jan-2011.

[13] Y. Shi, R. Li, Y. Xue, and H. Li, "Optimized Operation of Current-Fed Dual Active Bridge DC-DC Converter for PV Applications," *IEEE Trans. Ind. Electron.*, vol. 62, no. 11, pp. 6986–6995, Nov. 2015.

[14] L. Tarisciotti, P. Zanchetta, A. Watson, S. Bifaretti, and J. C. Clare, "Modulated Model Predictive Control for a Seven-Level Cascaded H-Bridge Back-to-Back Converter," *IEEE Trans. Ind. Electron.*, vol. 61, no. 10, pp. 5375–5383, Oct. 2014.

[15] L. Tarisciotti, P. Zanchetta, A. Watson, J. C. Clare, M. Degano, and S. Bifaretti, "Modulated Model Predictive Control for a Three-Phase Active Rectifier," *IEEE Trans. Ind. Appl.*, vol. 51, no. 2, pp. 1610–1620, Mar. 2015.

[16] L. Tarisciotti *et al.*, "Model Predictive Control for Shunt Active Filters With Fixed Switching Frequency," *IEEE Trans. Ind. Appl.*, vol. 53, no. 1, pp. 296–304, Jan. 2017.

[17] P. Karamanakos, T. Geyer, and S. Manias, "Direct model predictive current control of DC-DC boost converters," in *2012 15th International Power Electronics and Motion Control Conference (EPE/PEMC)*, 2012, p. DS2c.11-1-DS2c.11-8.

[18] F. M. Oettmeier, J. Neely, S. Pekarek, R. DeCarlo, and K. Uthaichana, "MPC of Switching in a Boost Converter Using a Hybrid State Model With a Sliding Mode Observer," *IEEE Trans. Ind. Electron.*, vol. 56, no. 9, pp. 3453–3466, Sep. 2009.

[19] K. Z. Liu and Y. Yokozawa, "An MPC-PI approach for buck DC-DC converters and its implementation," in *2012 IEEE International Symposium on Industrial Electronics*, 2012, pp. 171–176.

[20] O. Yade, J.-Y. Gauthier, X. Lin-Shi, M. Gendrin, and A. Zaoui, "Modulation strategy for a Dual Active Bridge converter using Model Predictive Control," in *2015 IEEE International Symposium on Predictive Control of Electrical Drives and Power Electronics (PRECEDE)*, 2015, pp. 15–20.

[21] P. Karamanakos, T. Geyer, and S. Manias, "Direct Voltage Control of DC–DC Boost Converters Using Enumeration-Based Model Predictive Control," *IEEE Trans. Power Electron.*, vol. 29, no. 2, pp. 968–978, Feb. 2014.

[22] H.-B. Shin, J.-G. Park, S.-K. Chung, H.-W. Lee, and T. A. Lipo, "Generalised steady-state analysis of multiphase interleaved boost converter with coupled inductors," *IEE Proc. - Electr. Power Appl.*, vol. 152, no. 3, p. 584, 2005.

[23] Y. A. Harrye, K. . Ahmed, G. . Adam, and A. . Aboushady, "Comprehensive steady state analysis of bidirectional dual active bridge DC/DC converter using triple phase shift control," in *2014 IEEE 23rd International Symposium on Industrial Electronics (ISIE)*, 2014, pp. 437–442.

[24] Hua Bai and C. Mi, "Eliminate Reactive Power and Increase System Efficiency of Isolated Bidirectional Dual-Active-Bridge DC–DC Converters Using Novel Dual-Phase-Shift Control," *IEEE Trans. Power Electron.*, vol. 23, no. 6, pp. 2905–2914, Nov. 2008.

[25] G. Xu, D. Sha, J. Zhang, and X. Liao, "Unified Boundary Trapezoidal Modulation Control Utilizing Fixed Duty Cycle Compensation and Magnetizing Current Design for Dual Active Bridge DC–DC Converter," *IEEE Trans. Power Electron.*, vol. 32, no. 3, pp. 2243–2252, Mar. 2017.

[26] J. Huang, Y. Wang, Z. Li, and W. Lei, "Unified Triple-Phase-Shift Control to Minimize Current Stress and Achieve Full Soft-Switching of Isolated Bidirectional DC-DC Converter," *IEEE Trans. Ind. Electron.*, vol. 63, no. 7, 2016.

[27] T. Dragicevic, "Model Predictive Control of Power Converters for Robust and Fast Operation of AC Microgrids," *IEEE Trans. Power Electron.*, vol. 33, no. 7, pp. 6304–6317, Jul. 2018.